A multi-objective design optimization strategy for acoustic/elastic metamaterials under impact loading

Azevedo Vasconcelos, Ana Carolina; Schott, Dingena; Jovanova, Jovana

Important note
To cite this publication, please use the final published version (if applicable).
Please check the document version above.

A multi-objective design optimization strategy for acoustic/elastic metamaterials under impact loading

Ana Carolina Azevedo Vasconcelos *, Dingena Schott, Jovana Jovanova [ID]

Faculty of Mechanical Engineering, Delft University of Technology, Mekelweg 2, 2628 CD Delft, The Netherlands

ARTICLE INFO

ABSTRACT

The use of optimization procedures for designing acoustic/elastic metamaterials (A/E MMs) has gained significant interest since they enable the efficient attainment of unique functionalities often contradicting. When it comes to vibration attenuation caused by mechanical stress waves, such as impact loads, the dynamic properties of A/E MMs are optimized so that their wave-control ability is maximized. However, the mechanical performance of A/E MMs during the propagation of such waves is normally not evaluated into the design optimization stages. This may compromise not only the load-bearing capacity of MMs, but also their ability in attenuating vibrations. To prevent such effects, we propose a design strategy that incorporates the stress analysis in the early design phase of A/E MMs subjected to an impact load. The effective mass density approach is applied, from which the vibration attenuation is identified at frequency ranges where the resonator moves out-of-phase in relation to the applied excitation. Regarding to the A/E MM mechanical behavior, maximum von Mises stress is calculated through the transient analysis of a unit cell array subjected to a dynamic load. A Pareto front shows a trade-off behavior between the A/E MM functionalities. With that, we emphasize the importance of incorporating the mechanical performance into the design stage of A/E MMs for vibration attenuation of structures undergoing high impact loads, such as installation of foundations by impact hammering. This brings A/E MMs closer to real applications involving energy filtering at specific frequencies from transient loads, designed in an optimized and efficient way.

1. Introduction

Metamaterials (MMs) refer to architected structures exhibiting unique effective properties that are not found in their constituent materials. Due to such properties, MMs have been widely explored for solving wave propagation problems. The sub-category of MMs possessing properties for manipulating mechanical waves is named as acoustic/elastic metamaterials (A/E MMs). These MMs are comprised of locally resonant periodic (or non-periodic) unit cells, which retain subwavelength frequency attenuation ranges (also known as resonant band gaps). The dynamic interaction between the local resonators and the propagating mechanical wave results in frequency-dependent effective properties, such as negative mass density [1], negative bulk modulus [2], and double negativity [3] (both mass density and bulk modulus have negative values). As a result of that, A/E MMs have been extensively investigated within the field of noise/vibration control [4–8].

Regarding to the attenuation of mechanical waves induced by dynamic loads (such as impact loads), some works reported the use of the dynamic effective properties of A/E MMs. For instance, Tan et al. (2014) [9] demonstrated numerically the attenuation performance of single- and dual-resonator models during the transmission of blast waves. Both models consisted of spring–mass systems retaining the negative effective density at two distinct frequencies. An experimental validation of A/E MMs for impact wave attenuation was presented by Khan et al. (2018) [10]. They showed a transmission reduction at the frequency related to the resonance of an unit cell made of aluminum and steel. The effective mass density of metapanels, a metamaterial-based sandwich structure, was also applied to attenuate blast waves [11]. Although these studies have developed A/E MM designs for impact load attenuation, a verification of their mechanical performance is still to be demonstrated. The lack of such analysis can result in two main drawbacks. First, the design may not resist the impact load due to the use of thin elements and significantly large masses to create the subwavelength resonant band gap. Second, the deformation of such MMs can modify their dynamic effective properties. In the works reported by Wang et al. (2014) and Bertoldi et al. (2017) [12,13], the buckling effect was exploited to tune the band gaps of acoustic MMs. It was highlighted that the pre-deformation of

---

* Corresponding author.
E-mail address: a.c.azevedovasconcelos@tudelft.nl (A.C. Azevedo Vasconcelos).

MMs can induce the band gap formation at different frequency ranges. Including the mechanical performance of A/E MMs in their design stage is crucial to retain the MM effective properties for the desired application.

The design of A/E MMs with a desired functionality typically relies on experiments or trail-and-error approaches. Depending on the complexity of the geometry, the required manufacturing constraints, and the method used to determine the A/E MM's effective properties, the current iterative design process can be computationally expensive and time consuming. To avoid that, optimization techniques have been explored to systematically design A/E MMs, i.e., by implying the desired functionalities and respecting the imposed geometric constraints in the design stage. Gradient-based methods are commonly used to optimize A/E MMs. For instance, Oh et al. (2015) [14] conducted topology optimization using the homogenization method to maximize the operating frequency range of hyperbolic elastic MMs. Topology optimization has also been used to design acoustic MMs slabs exhibiting a prescribed negative refraction at a specific incidence angle and frequency [15]. Lu et al. (2013) [16] proposed a level-set based topology optimization to design acoustic MMs with negative bulk modulus at specific frequencies. At the same direction, Noguchi et al. (2022) [17] designed acoustic labyrinthine MMs with a negative refractive index by means of level-set based topology optimization. Since gradient-based methods are not effective for non-convex problems, suboptimal configurations (local minima) may be found. In a worst scenario, the solution can diverge in case of the initial design is not well selected. Furthermore, gradient-based methods require the sensitivity of the fitness function with respect to some design variable, which could be a challenge task for some optimization problems. To avoid that, efforts have been devoted to design MMs via non-gradient-based methods such as evolutionary methods; these algorithms borrow concepts from evolutionary biology—a population of individuals evolves over generations so as to optimize a fitness function (it is worth noticing that evolutionary algorithms may not guarantee a global solution, since there is no optimality criterion). To mention some works, Dong et al. (2017) [18] introduced a topology optimization approach to design two-dimensional single-phase elastic MMs with double-negative effective material properties by using the single-objective genetic algorithm (GA). Shape optimization approaches combining effective properties and GA have also been introduced to design single-phase chiral elastic MMs [19]. Broadband vibration attenuation of one-dimensional and two-dimensional meta-structures was achieved via optimization procedures based on genetic algorithms [20–23]. In the field of active metamaterials, whose properties are actively adjusted by external stimuli, genetic algorithm procedures have been employed to achieve improved vibration suppression [24–26]. Besides that, evolutionary algorithms can take full advantage of parallel computing—reducing significantly the computational time—, since the fitness evaluation of all individuals is independent. Despite the significant contributions made by GA, investigations concerning the study of vibration attenuation and mechanical performance relation in early design stage remains still unexplored.

In this paper, we investigate the influence of integrating the mechanical performance into the design process of A/E MMs through a multi-objective optimization using GA. The unit cell's geometry is initially parameterized, from which a vector of design variables is defined and employed to update the two fitness functions required in this optimization problem; the first related to the vibration attenuation analysis, while the second evaluates the maximum stress due to an impact load. Adequate geometric constraints are defined so that the manufacturing of the optimized MMs is feasible. The multi-objective optimization provides in the end a Pareto front, which shows a set of non-dominated optimal solutions. We analyze the trade-off behavior between mechanical and vibration attenuation performance and discuss the importance of incorporating these features into the design stage of A/E MMs. Through such multi-objective design optimization, the A/E

MM can be used for attenuating vibrations at specific frequencies of structures undergoing high amplitude impact loads, such as foundations installed in onshore or offshore environment through an impact hammer and structures exposed to shock waves.

2. Performance indicators of acoustic/elastic metamaterials

In this section, the evaluation of the vibration attenuation and mechanical performance of A/E MMs is introduced. The unit cell geometry used in this work is initially described and its dynamic features are investigated. Finally, a strategy to determine the stresses caused by an impact load is presented.

2.1. Unit cell model and dispersion curves

The dynamic characteristics of A/E MMs will provide information about the vibration attenuation functionality. The characterization starts by initially defining the unit cell design. The design steps of the unit cell are presented in Figs. 1a and b. A square unit cell with side length a contains a resonator, with a mass represented by a rounded-vertex square structure of length $2R_2$ containing four rectangular-shape cavities of length l_g and width w_g, and four identical beams with length l_b and width w_b. The round shape of the square vertices is introduced by a fillet with radius R_2^f. The resonator is embedded in an external rounded-vertex square frame of size $2R_1$ containing a fillet of radius R_1^f. A fillet r_f was also included in the edges connecting the beams to the external frame. The unit cell has a thin out-of-plane thickness t_c, enabling the assumption of plane stress analysis. We consider an unit cell made of Nylon, with properties Young's modulus $E_n = 2$ GPa, density $\rho_n = 1150 \, \text{kg/m}^3$, and Poisson's ratio $v_n = 0.4$.

Dispersion curves are commonly used to evaluate the dynamic features of A/E MMs, since they show the relation between the wavelength and frequency of a wave propagating in the medium. Consequently, band gaps can be identified as the frequency zones with no dispersion curves, which means no wave propagation. For that purpose, here we consider an infinite 2D medium formed by periodically repeated unit cells presented in Fig. 1b. The periodicity is introduced along the in-plane boundaries of the unit cell and it is conducted by Bloch–Floquet theorem, which states that the displacement field $\mathbf{u}$ satisfies

$$\mathbf{u}(\mathbf{x} + \mathbf{a}, \mathbf{k}) = \mathbf{u}(\mathbf{x}, \mathbf{k}) \, e^{i(\mathbf{k} \cdot \mathbf{a})}, \tag{1}$$

where $\mathbf{x}$ is the position vector, $\mathbf{a}$ is the lattice vector of the periodic material, $\mathbf{k}$ is the wave vector of the propagating wave, and $i = \sqrt{-1}$. Due to the periodicity of the unit cell, the vector $\mathbf{k}$ is defined at the edges of the irreducible Brillouin zone (green triangle in Fig. 1c). The band structure is obtained by solving the following eigenvalue problem

$$(\mathbf{K}(\mathbf{k}) - \omega^2 \mathbf{M})\mathbf{u} = \mathbf{0}, \tag{2}$$

where $\mathbf{K}(\mathbf{k})$ and $\mathbf{M}$ are, respectively, the global stiffness and global mass matrices, and ω is the angular frequency of the propagating wave. To investigate the mechanism of local-resonant band gaps, the band structure is determined for an unit cell with the following geometric parameters: $a = 0.042$ m, $R_1 = 0.47a$, $R_2 = 0.46a$, $w_b = 1$ mm, $l_g = 0.07a$, $w_g = 0.1a$, $l_b = R_2 - l_g$, $R_1^f = 0.85R_1$, $R_2^f = 0.85R_2$, $r_f = 0.5$ mm, and $t_c = 10$ mm. The commercial software COMSOL Multiphysics is used to calculate the band structure. The first six band modes are depicted in the left of Fig. 1c, with abscissas $\Gamma - X - M - \Gamma$. A band gap ranging from 488 Hz to 556 Hz is identified (gray rectangle) and its flat edges—or, close-to-zero group velocity—indicate that it results from local resonance [4]. This can be observed from modes M_1 and M_2, where the motion is mostly confined to the resonator.
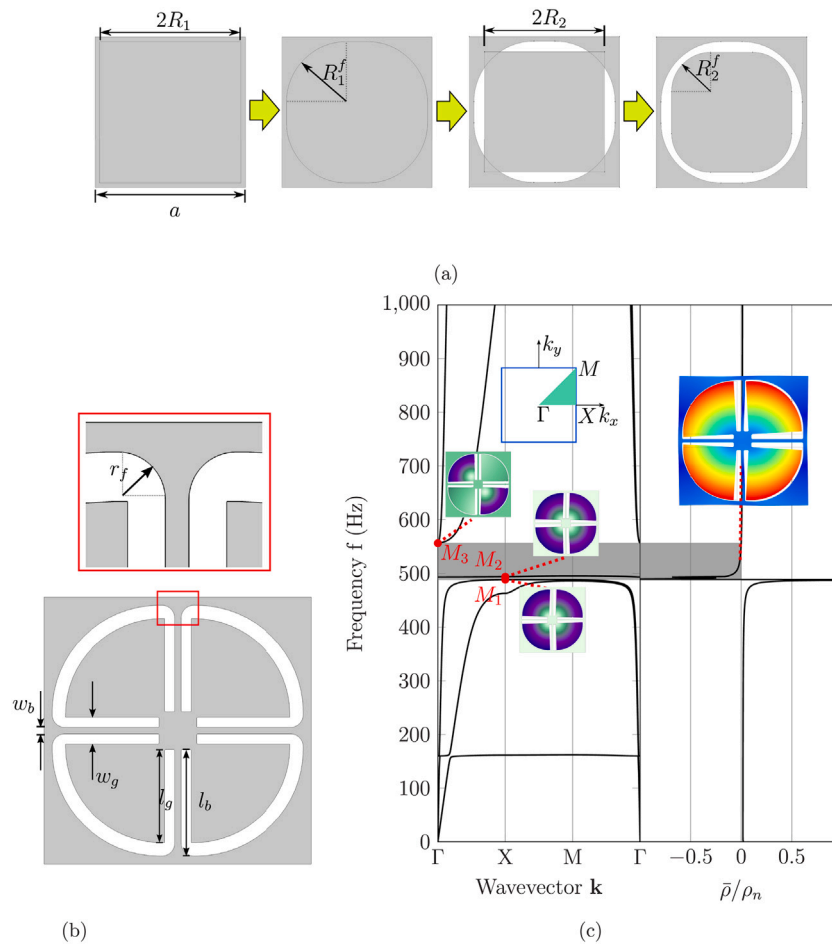
Fig. 1. (a) Steps for definition of the external frame of the unit cell and the resonator mass. Fillets R_1^f and R_2^f are used to create the round shape of the square's vertices. (b) Final design of unit cell with remaining geometric parameters. (b) Band structure and effective mass density of the initial unit cell design. The band structure shows the first six modes of the periodic unit cell for a finite set of wavevectors **k** along the IBZ (green triangle), where two band gaps are observed. The gray rectangle indicates the resonant band gap. The inset highlights the modes (M_1, M_2, and M_3) identified at the band gap edges and the displacement field obtained by exciting harmonically the unit cell at a frequency of 525 Hz.
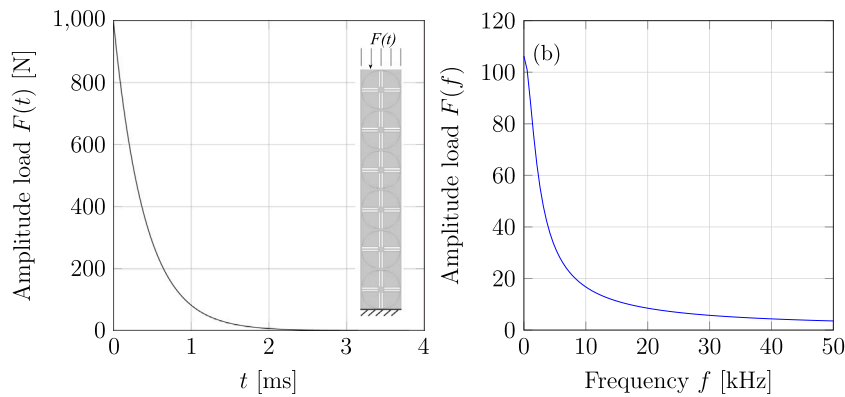
Fig. 2. (a) Impact load used in the transient analysis; and (b) frequency spectrum of the corresponding load.
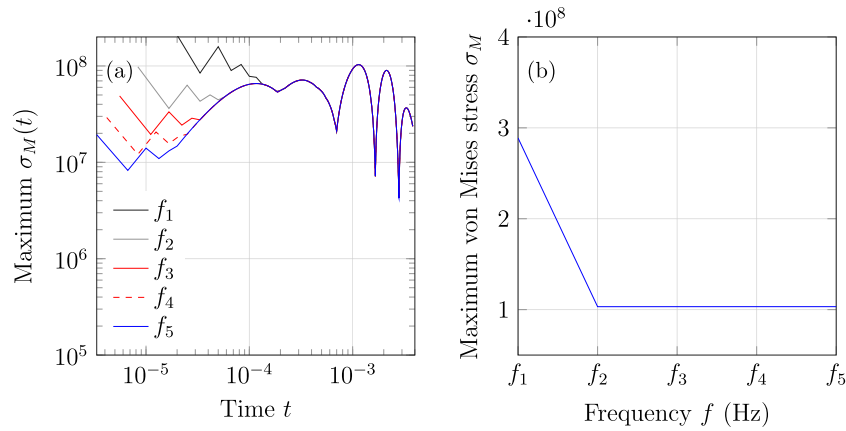
2.2. Effective mass density

Under the long wavelength assumption, whereby the phase displacement difference among boundaries is ignored [27], the effective mass density of the unit cell can be determined. To that end, a harmonic prescribed displacement is applied to the four external boundary edges of the unit cell, and the corresponding reaction forces are evaluated by

$$\left(\mathbf{K} - \omega^2 \mathbf{M}\right) \mathbf{U} = \mathbf{F}, \tag{3}$$

where ω is the frequency of the driving excitation, and **U** and **F** are the global displacement and external force vectors, respectively. The effective mass density is then calculated by averaging the reaction force with the acceleration, in all edges, as [28]

$$\bar{\rho}(\omega) = -\frac{1}{V} \frac{F_b}{\omega^2 U_b}, \tag{4}$$

where F_b and U_b are the averaged reaction force and displacement in the edges, respectively, and V is the volume of the unit cell.

Fig. 3. (a) Maximum von Mises stress in function of time for different maximum frequencies f_i. (b) Maximum von Mises stress value obtained from transient simulations for each f_i.

To further understand the physics behind the effective mass density, a harmonic prescribed displacement in the x direction of amplitude $u_x = 0.1$ mm is applied at the external boundaries of the unit cell described in Section 2.1. The reaction forces are obtained by Eq. (3) and replaced in Eq. (4) to determine the effective mass density. The right curve in Fig. 1c shows the frequency as a function of the normalized effective mass density (EMD) $\bar{\rho}/\rho_n$ of the proposed unit cell. We notice that the normalized EMD is slightly constant until 400 Hz. Close to the resonant frequency of the unit cell, the EMD increases to an infinite positive value and suddenly drops to an infinite negative value. After that, the EMD increases and becomes constant again. The inset shows the displacement field of the unit cell at $f = 525$ Hz, where the EMD is negative. At such frequency, the positive external loads induce an out-of-phase motion of the resonator, which prevents the wave energy to propagate through the structure [29].

From such analysis, it is worth noticing that the negative EMD region starts nearby the frequency of the lower band gap's edge. Since the determination of the EMD is less computationally demanding than the band structure—here it requires solving the eigenvalue problem stated in Eq. (2) with Bloch–Floquet periodic BC for a finite set of vectors along the IBZ (Fig. 1c)—the EMD was chosen as the method to optimize the unit cell's band gap.

2.3. Transmission loss diagram

We have shown that the determination of the band gap by means of dispersion curve analysis and the effective mass density requires some assumptions; in the first analysis, we assume that the unit cell is periodically repeated in a infinite domain, while in the second, the long wavelength assumption is used. To investigate the attenuation performance of the metamaterial in a finite domain, a transmission loss diagram is numerically computed. Here, we consider a plate containing a finite number of unit cells. The excitation is a sinusoidal horizontal prescribed displacement $u_I(\omega)$ of amplitude 0.1 mm, which is applied at a point before the unit cell arrangement. The output displacement $u_O(\omega)$ is then measured at a point after such arrangement. To reduce the effect of reflected waves, perfectly matched layers (PML) were included at the plate ends. The transmission loss (TL) is then computed by

$$\mathrm{TL}(\omega) = 20 \log_{10} \frac{u_O}{u_I}, \tag{5}$$

2.4. Determination of transient stress

This section introduces the finite element model used for calculating stresses induced by an impact load. Fig. 2 depicts the model, comprising an array of identical unit cells subjected to a transient

load at the top edge, with zero displacement prescribed at the bottom edge. The load function is represented as $F(t) = F_0\, e^{-t/0.0001}$, where $F_0 = 1$ kN is the maximum load amplitude and t is the time in seconds. As systems without damping may exhibit oscillatory behavior under impact loads, especially high-frequency content that leads to noisy responses, this would require more iterations and smaller time steps, slowing numerical convergence and increasing computational time. To enhance the convergence, numerical damping is introduced as small Rayleigh damping coefficients, $\alpha = 0$ and $\beta = 1e{-}4$ (material damping has demonstrated influence on the vibration attenuation performance, therefore small values are also used in this work to restrict the vibration attenuation to the resonance effect of the unit cell [30]). The time step Δt and the maximum element mesh size e_{max} for the transient problem are determined based on the maximum frequency to be solved, f_{max}. Consequently, Δt is set as $1/(60 f_{max})$, and e_{max} is defined as $c/(6 f_{max})$, where c represents the wave speed in the medium and the number 6 indicates the minimum number of finite elements per wavelength. The end time for each transient analysis calculation is set at 0.0038 s to also capture the response of reflected elastic waves.

From Fig. 2b, it is noticed that the energy content of the impact is concentrated within frequencies below 10 kHz. To accurately determinate the maximum frequency, Fig. 3a depicts the maximum transient von Mises stress response for five maximum frequency values ($f_i = [1, 2, 3, 4, 5]$ kHz, where $i = 1, \ldots, 5$). Notably, selecting a maximum frequency $f_{max} = f_2 = 2$ kHz yields a favorable stress response, since frequencies exceeding 2 kHz provide comparable values of maximum von Mises stress, as indicated in Fig. 3b.

3. Design optimization strategy

In this work, the performed optimization updates the unit cell design according to its geometric parameters. Due to the high complexity of the unit cell geometry (see Fig. 1a), the geometric parameters that contribute the most to the band gap performance are carefully selected to constitute the design variable (DV) vector. The selection is conducted through a parametric EMD analysis of the main resonant elements. A parametric sweep is defined according to the possible minimum and maximum dimensions for each geometric feature. Since only three parameters are used to define the external frame (R_1, R_1^f and r^f) they are directly considered as DVs. It is worth to mention that the size of the unit cell a will remain constant, since our aim is to explore the possible resonator's shape within a fixed frame.

Fig. 4 shows the relation between the band gap's width and the variation of the resonator's size R_2, the beam's width w_b, the cavity's position l_g, and the cavity's width w_g. From those parameters, the band gap is less sensitive to the beam's width variation, which is due to the limited size range (the beams cannot be thinner than the manufacturing
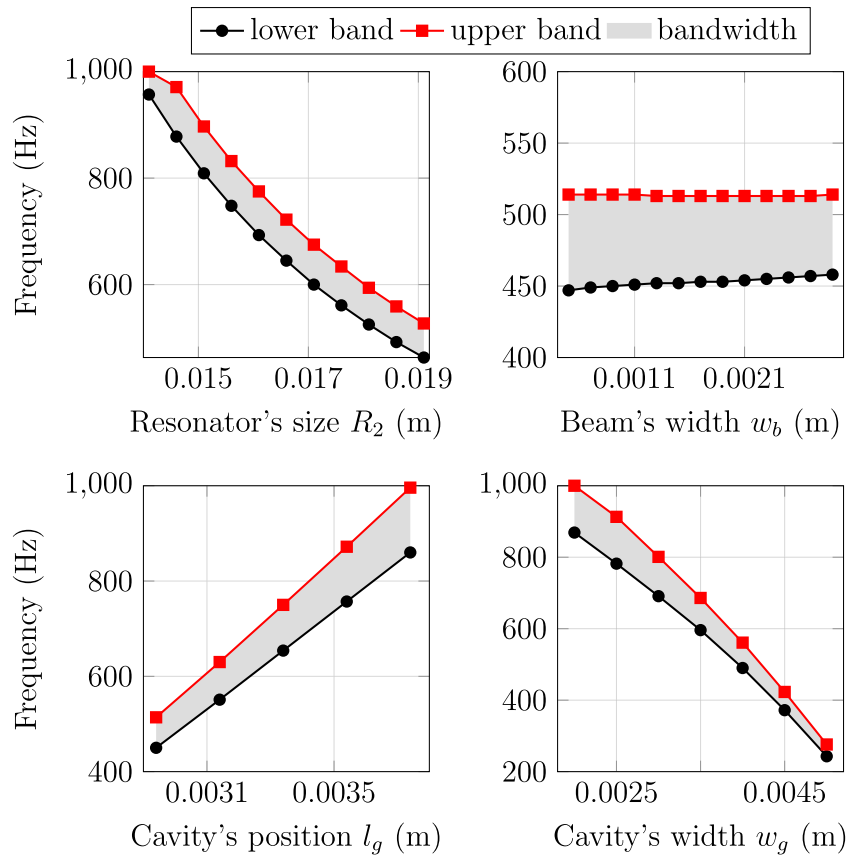
Fig. 4. Variation of the bandwidth and central frequency of the BG for different ranges of the resonator's size R_2 (top left), the beam's width w_b (top right), the cavity's position l_g (bottom left), and the cavity,s width w_g (bottom right).

resolution nor too large to avoid contact with the resonator's mass). While the increase of R_2 and w_g results in a decrease of the central frequency of the band gap, the opposite effect is observed when the cavity's position increases—i.e., when the beam's length is shorter. From these observations, R_2 (and its fillet R_2^f), l_g and w_g were chosen as design variables for further optimization.

GAs have been widely employed to solve complex optimization problems, specially multi-modal ones containing several local minima. Unlike classical optimization methods, which rely on deterministic operators, GAs use stochastic operators that can explore better the search space to achieve the optimal solution. The algorithm works by initially defining a population P_0 containing I_0 individuals randomly generated [31]. Then, the algorithm starts a loop over a maximum number of generations G_m. In each iteration, the population is evaluated according to a defined objective function. The individuals containing lower fitness values are chosen by means of a selection function to constitute the parent population (P_p). The genetic operators crossover and mutation are applied to the individuals of P_p to create the individuals of the next iteration (offspring population P_o). The mutation operator makes random changes in a single individual from P_p, while the crossover operator combines information of two individuals from P_p. The algorithm ends when one of the stopping criteria (for instance, maximum number of generations, maximum computational time or tolerance on the objective function) is reached.

Since in this work two independent parameters are investigated (the negative mass density and the maximum stress), a GA-based multi-objective optimization strategy is used. In this case, distinct solutions may generate a trade-off behavior between the objectives, which means that the improvement of one objective only occurs when compromising the other objective. This is shown in the end of the optimization by means of a Pareto front, which represents a set of optimal solutions in

the space of objective functions. From such solutions, we select the one that is most suitable for a desired application.

The multi-objective optimization problem is then stated as,

$$\min \quad \Phi = (\phi_1(\mathbf{d}), \phi_2(\mathbf{d}))$$

$$\text{subjected to} \quad 17.44\,\text{mm} \leq R_1 \leq 19.74\,\text{mm},$$
$$16.60\,\text{mm} \leq R_2 \leq 19.32\,\text{mm},$$
$$4.2\,\text{mm} \leq w_g \leq 4.5\,\text{mm},$$
$$2.94\,\text{mm} \leq l_g \leq 3.94\,\text{mm},$$
$$0.1\,\text{mm} \leq r_f \leq 1\,\text{mm},$$
$$98.7\,\text{mm} \leq R_1^f \leq 107.52\,\text{mm},$$
$$96.6\,\text{mm} \leq R_2^f \leq 100.8\,\text{mm},$$
$$R_2 - R_1 \leq 0,$$
$$R_1^f - R_2^f \leq -1\,\text{mm},$$

(6)

where $\mathbf{d}$ is the vector of design variables defined as $\mathbf{d} = [R_1, R_2, w_g, l_g, r_f, R_1^f, R_2^f]$. The set of geometric constraints exhibits both the geometric bounds and the inequality constraints so that a gap of 1 mm is kept between two parameters. The first function ϕ_1 is related to the band gap optimization and it minimizes the ratio between the central frequency of the band gap and its bandwidth, i.e,

$$\phi_1(\mathbf{d}) = \frac{0.5(f_2 + f_1)}{f_2 - f_1}, \tag{7}$$

f_1 and f_2 represent, respectively, the lower and upper frequencies defining the band gap (the negative EMD region). The second objective function is defined such as the ratio between the maximum transient von Mises stress and the yield stress is minimized. Therefore,

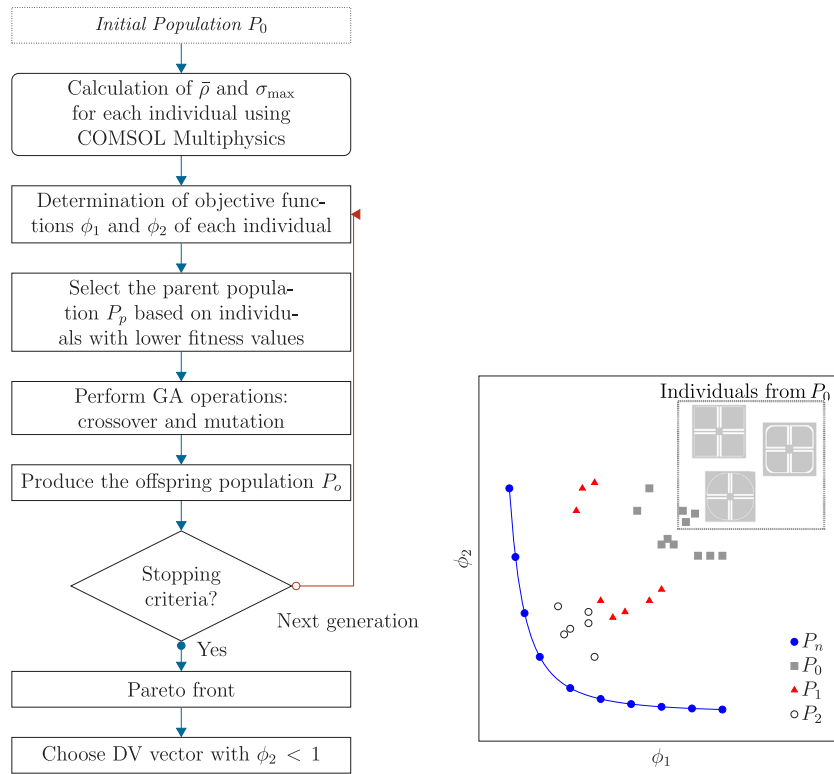$$\phi_2(\mathbf{d}) = \frac{\sigma_{\max}}{\sigma_y}, \tag{8}$$

Fig. 5. Flowchart of the design optimization used to evaluate the trade-off behavior, which gives in the end a Pareto front with optimal solutions. On the right, it is shown a schematic of the Pareto front evolution through generations. The inset highlights three unit cells randomly generated in the first population P_0.

where σ_y is the yield stress of the constituent material (for Nylon $\sigma_y = 71.7$ MPa).

A flow chart describing each step of the multi-objective optimization is presented in Fig. 5. The optimization problem is solved using Matlab's built-in function *gamultiobj*. It starts by calculating the EMD $\bar{\rho}$ and the maximum von Mises stress σ_{max} for each individual of the initial population P_0 via COMSOL Multiphysics. By using the GA operations, the population evolves until it reaches the maximum number of generations or the function tolerance, from which a Pareto front is obtained (refer to schematic on the right from Fig. 5). We select then the set of DVs with $\phi_2 < 1$ that is most suitable for a desired application.

4. Multi-objective design optimization results and discussion

In this section, the trade-off behavior will be explored by performing the multi-objective optimization described in Section 3. Preliminary simulations revealed that a population size of 250 effectively provides a Pareto front with a sufficient amount of optimal solutions that will be further verified. The optimization stops when it reaches one of the stopping criteria; here it has been considered the maximum number of generations, which is equal to 20, and a function tolerance of 1e−3, which indicates the minimum change in each objective function value that should occur between generations. The individuals constituting the parent population are chosen by the tournament function and the mutation children are produced by the mutation power function. The crossover fraction used to create the next generation is set to 0.8.

Fig. 6a shows the cumulative optimal points in gray for generations $G < 20$ and the optimal Pareto front in black when $G = 20$. Notably, the front depicts the trade-off between the objective functions, i.e., the improvement of ϕ_1 only occurs with a decrease in ϕ_2 and vice-versa. The gray area in the figure highlights the region of unfeasible designs, where the linear regime condition is violated, as proposed by Eq. . Three individuals on the Pareto front are identified, labeled P_A, P_B, and P_C. The individual P_A indicates the case with the lowest ratio between

Table 1
Band gap features – central frequency and bandwidth – for individuals P_A, P_B, and P_C illustrated in Fig. 7.

| Individual	Central frequency [Hz]	Bandwidth [Hz]	Objective function ϕ_1
P_A	616	105	5.867
P_B	704	94	7.489
P_C	643	100	6.430

the central frequency of the band gap and its bandwidth; the second individual P_B represents an unit cell containing the lowest levels of von Mises stress; individual P_C highlights the limit case, i.e, the array formed by the optimized unit cell is near the limit of elastic regime.

The EMD curves of the three individuals are shown in Fig. 6b with their respective band gaps highlighted in their corresponding colors. The individual P_C exhibits a band gap within ranges of [593 Hz, 693 Hz] (shaded green area), while individuals P_A and P_B demonstrate band gaps within the ranges of [564 Hz, 669 Hz] (shaded red area) and [657 Hz, 751 Hz] (shaded blue area), respectively. A comparison of the central frequency and bandwidth of the band gaps for these three individuals are indicated in Table 1. As expected by the obtained objective function ϕ_1, individual P_A demonstrates the best optimized band gap, with the lowest central frequency and largest bandwidth, followed by individuals P_C and P_B. Such band gaps are also identified in the dispersion curves depicted in Fig. 7, where modes at the flat edges delineating the band gaps ($A_1, A_2, B_1, B_2, C_1, C_2$) indicate the resonant behavior of the internal structure.

To corroborate that the optimized unit cells effectively attenuate vibrations within the frequency ranges in the EMD curves, transmission loss diagrams are calculated. As illustrated in Fig. 8, these diagrams correspond to three plates, each composed of the unit cells P_A, P_B, and P_C. Across all diagrams, a discernible reduction in transmission occurs with the band gaps identified in Figs. 6b and 7. Notably, the peaks situated at the lower edges of the band gaps emphasize the resonance
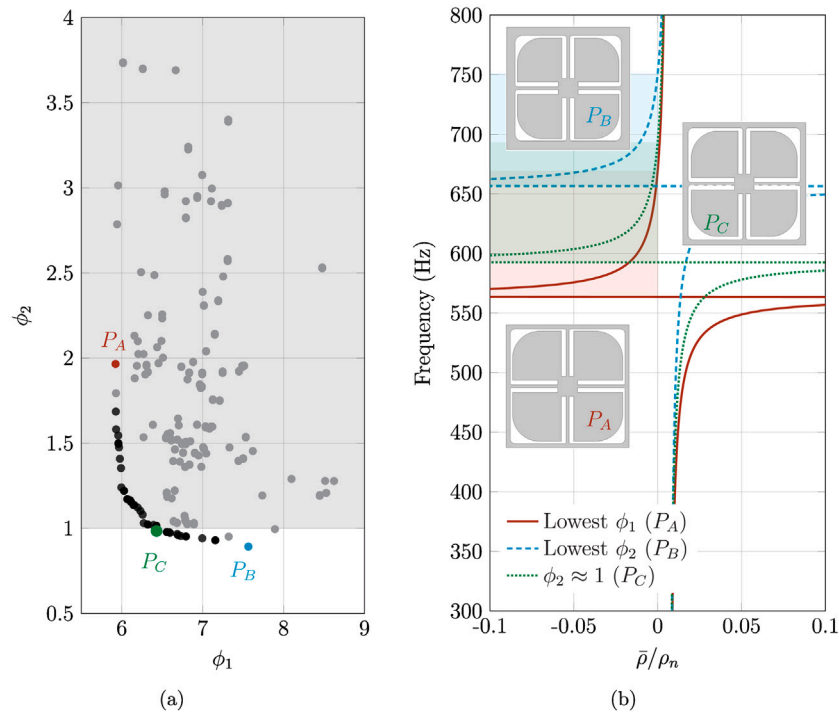
Fig. 6. (a) Optimal Pareto front obtained by solving the multi-objective optimization problem (black dots) and cumulative optimal solutions from previous generations (gray dots) with uniform beams. Individuals P_A, P_B, and P_C highlights the cases with lowest ϕ_1, lowest ϕ_2, and ϕ_2 close to 1, respectively. (b) Optimized EMD for individuals P_A, P_B, and P_C with their corresponding band gaps highlighted by the shaded areas and their unit cell designs. (For interpretation of the references to color in this figure legend, the reader is referred to the web version of this article.)
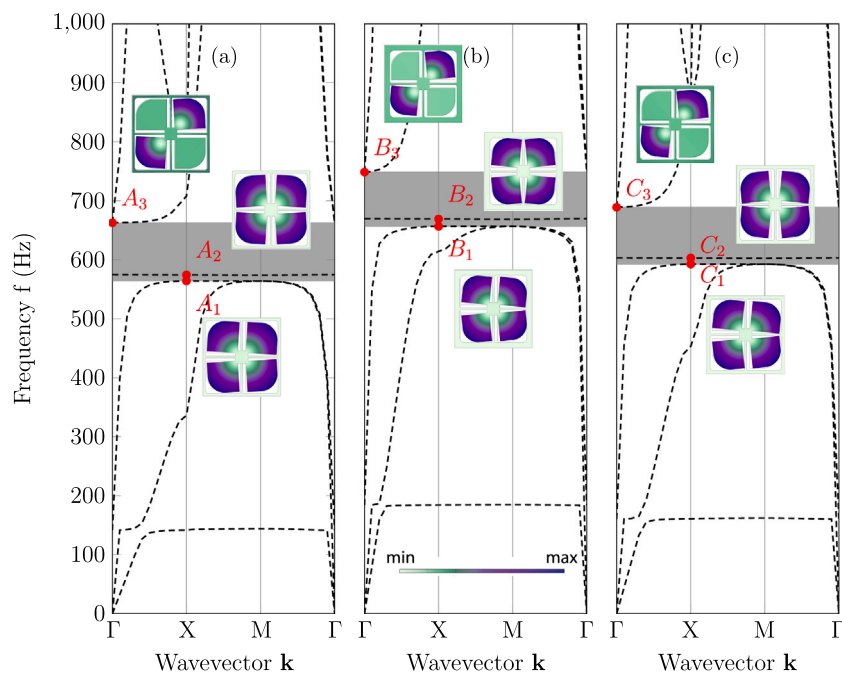
Fig. 7. Dispersion curves of the selected individuals (a) P_A, (b) P_B, and (c) P_C, respectively, from the Pareto front presented in Fig. 6. Complete band gaps are colored in gray. The inset shows the deformation motion of the unit cell at the flat edges defining the band gaps. (For interpretation of the references to color in this figure legend, the reader is referred to the web version of this article.)
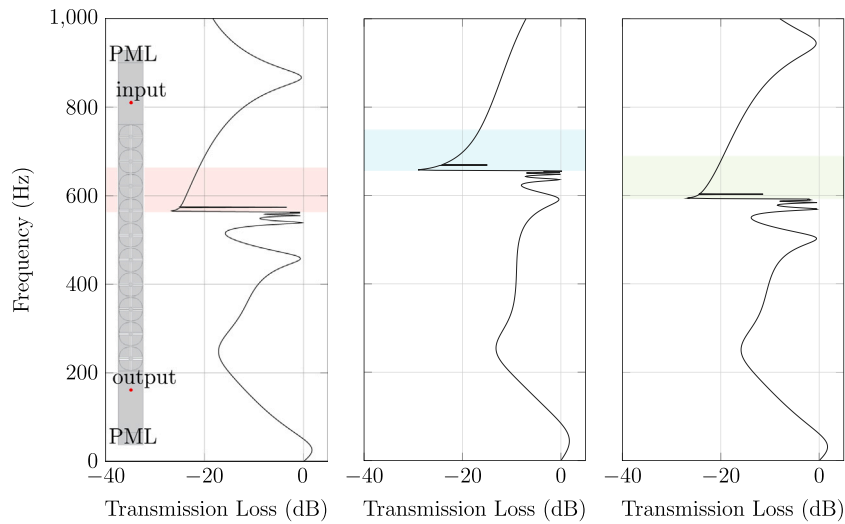
Fig. 8. Transmission loss diagrams for metamaterial plates containing unit cells P_A (left), P_B (middle), and P_C (right) presented in Fig. 6. The shaded areas indicate the band gap identified by the dispersion curves in Fig. 7 and the asymmetric peaks indicate the wave attenuation due to the unit cells' resonance. The inset shows a metamaterial plate for determination of the transmission loss diagram. A horizontal prescribed displacement is applied at the input and the resulting horizontal displacement is measured at the output. Perfectly matched layers are applied in the plate's ends to reduce the wave reflection.
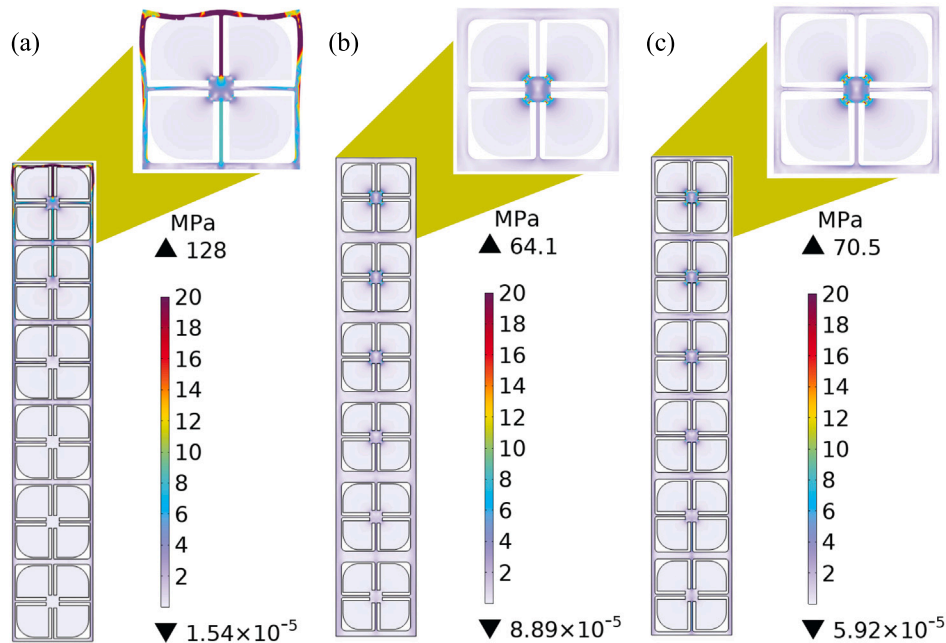

Fig. 9. von Mises stress field obtained in transient analysis of arrays formed by unit cells (a) P_A (b) P_B, and (c) P_C presented in Fig. 6. The stress fields were selected at time steps occurring the maximum von Mises stress for each array. The colormap indicates the variation of Von Mises stress with minimum and maximum values indicated by the triangles. (For interpretation of the references to color in this figure legend, the reader is referred to the web version of this article.)

as the mechanism of attenuation, consistent with the discussion in [32]. This analysis thus demonstrates the feasibility of optimizing band gaps through EMD calculation.

We evaluate the significance of integrating stress analysis into the MM design process. Fig. 9 illustrates the time step corresponding to the maximum transient von Mises stress within the arrays formed by unit cells P_A, P_B, and P_C. In Fig. 9a, the unit cell P_A comprises a large mass linked to a slender frame through thin beams, resulting in high stress concentration at the connection of these elements. Conversely, Figs. 9b and c indicate maximum stress values below the yield stress of Nylon for arrays formed by P_B and P_C, respectively. While traditional optimization may provide the design of unit cell P_A due to its superior attenuation performance, it would not be indicated in scenarios involving high impact loads.

In Fig. 4, we have shown that the band gap formation is less sensitive to the variation of the beam's width. However, the investigation of beams with variable cross-section was not explored. To that end, we will study the influence of non-uniform beams on the vibration attenuation and mechanical performance of the MM. Two geometric parameters will then define the variation of the beam's width: w_b and w_b^*; the first parameter defines the width of the beam's end connected to the mass while the second defines the width of the beam's end connected to the external frame. The new set of design variables is then defined as $DV_3 = [R_1, R_2, w_b, r_f, R_1^f, R_2^f, w_b^*]$. Geometric constraints for w_b^* and w_b are defined as $0.3\,\text{mm} \leq w_b^* \leq 2\,\text{mm}$ and $0.5\,\text{mm} \leq w_b \leq 3\,\text{mm}$, respectively. Fig. 10 highlights the Pareto front for the entire population after 20 generations, and the EMD for the three selected Pareto points, where the unit cells are illustrated in Fig. 10b. Here we
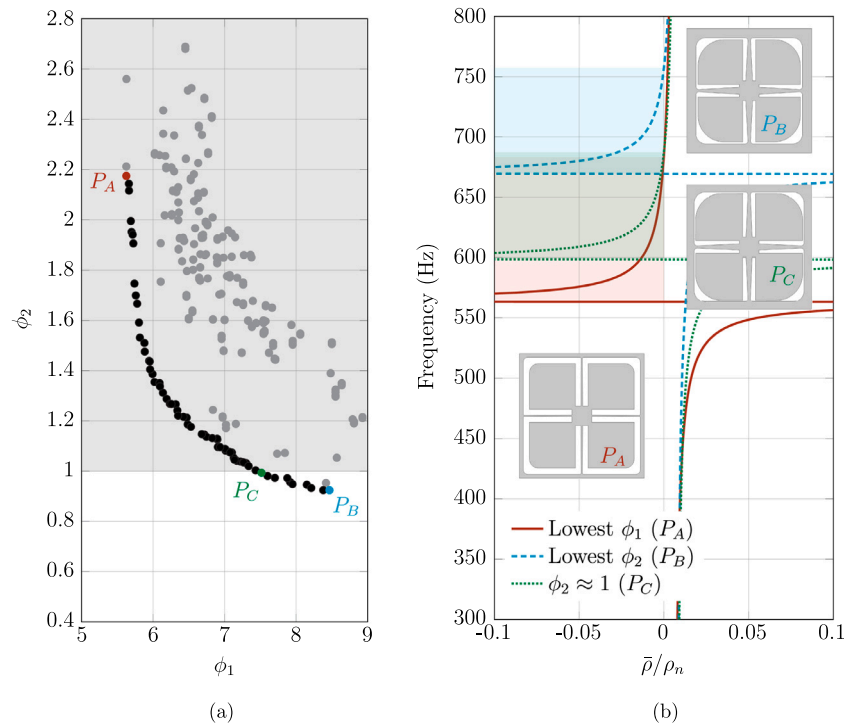
Fig. 10. (a) Optimal Pareto front obtained by solving the multi-objective optimization problem for an unit cell containing non-uniform beams. Individuals P_A, P_B, and P_C highlights the cases with lowest ϕ_1, lowest ϕ_2, and ϕ_2 close to 1, respectively. (b) Optimized EMD for individuals P_A, P_B, and P_C with their corresponding band gaps highlighted by the shaded areas and their unit cell designs. (For interpretation of the references to color in this figure legend, the reader is referred to the web version of this article.)

Table 2
Band gap features – central frequency and bandwidth – for individuals P_A, P_B, and P_C illustrated in Fig. 11.

Individual	Central frequency [Hz]	Bandwidth [Hz]	Objective function ϕ_1
P_A	623.5	119	5.239
P_B	713.5	87	8.201
P_C	643	88	7.307

notice a clear distinction among the beam shape of the three points; while point P_B explores the non-uniformity of the beams to reduce the stress concentration, point P_A still shows the use of beams with constant width to obtain the best band gap. By observing the unit cell of point P_C, we realize a combination of the two previous points—the non-uniformity is less apparent in comparison to point P_B, however, still notorious to reduce the stress (refer to Fig. 12).

A comparison of the central frequency and bandwidth of the band gaps for these three individuals are indicated in Table 2. As expected, individual P_A demonstrates the best optimized band gap, with the lowest central frequency and largest bandwidth. Although, individuals P_B and P_C have similar bandwidth, the central frequency of individual P_C is lower than P_B. The band gaps delineated in Fig. 10b are also evident in the dispersion curves depicted in Fig. 11. Interestingly, the dispersion curve of unit cell P_A depicts a negative slope, although attributed to a shear mode of the unit cell (as indicated by A_2). Additionally, the mode shapes at the lower edges of each band gap (A_1, A_3, B_1, B_2, C_1, and C_2) indicate the resonant behavior inherent in the internal structure of the unit cell.

Fig. 12 illustrates the time step corresponding to the maximum transient von Mises stress within the arrays formed by non-uniform unit cells P_A, P_B, and P_C. Despite unit cell P_A displaying a band gap with the lowest central frequency (as indicated in Figs. 10b and 11, the transient analysis reveals a maximum von Mises stress of 157 MPa (Fig. 12a). This value exceeds twice the yield stress of Nylon, while acceptable stress levels are observed within the arrays illustrated in Figs. 12b and c. Consequently, MMs formed by unit cells of configuration P_A may be unfeasible when subjected to high impact loads. Therefore, unit cell

configurations P_B and P_C are recommended, given their maximum von Mises stresses of 57.8 MPa and 63.3 MPa, respectively.

As in the previous analysis, we also verify the vibration attenuation functionality of plates formed by the unit cells containing non-uniform beams. The transmission loss diagrams of such plates are shown in Fig. 13. In all diagrams, it is realized a transmission attenuation at the same frequency ranges of the band gaps identified in Figs. 10 and 11.

From the analyses of the individuals highlighted in the Pareto fronts from Figs. 6 and 10, we can observe a certain trend in how the unit cells are designed. When considering the solutions where the first fitness functions ϕ_1 are dominant (points P_A), the unit cell is usually formed by thin uniform beams, the frame is narrow, and the fillet at the connection between the frame and the beams has a small radius. We also notice that the resonator's mass tends to fit the frame's cavity, i.e., the mass is maximized. For the unit cells related to the points P_B (dominant solution is associated to the second fitness function ϕ_2), the frame and the beams are thicker and non-uniform, the fillets have larger radius, and the resonator's mass is smaller. This explains the generation of higher-frequency band gaps. Lastly, we notice that the unit cells associated to the points P_C are a combination of the two previous points. The beams' width of such unit cells can slightly vary to create the low-frequency band gap and to have a better stress distribution. Moreover, the external frame is wide enough to ensure less deformation. Such design aspects will guarantee the overall performance of the A/E MM structure.

Conclusions

This paper investigates the critical role of stress analysis in the design of impact-loaded A/E MMs, emphasizing its importance in ensuring optimal vibration attenuation and mechanical performance at the early design phase. Failure to evaluate structural integrity during the design process of A/E MMs may lead to fragile designs prone to break before achieving desired vibration attenuation. To mitigate this risk, we proposed a design optimization strategy that integrates stress analysis into A/E MM design to attenuate vibration induced
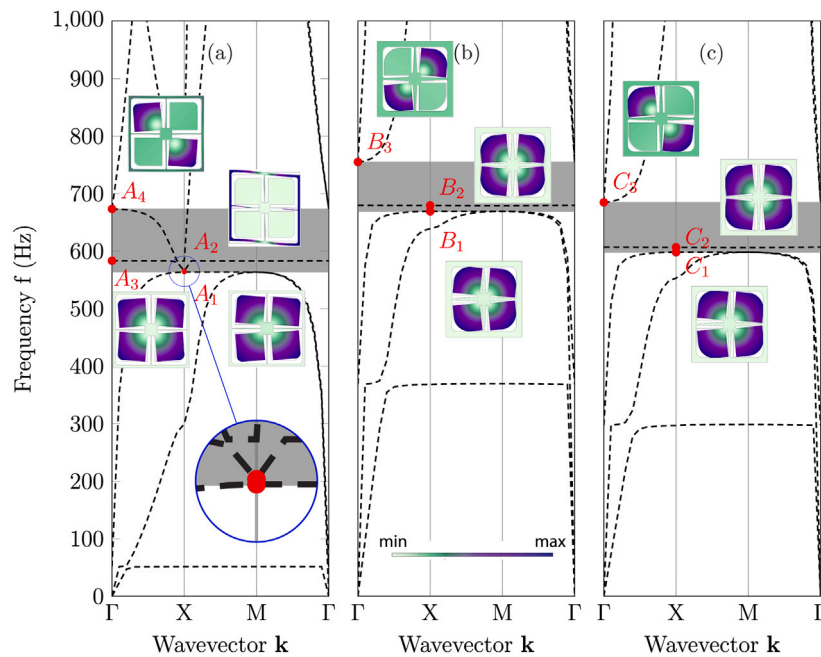
Fig. 11. Dispersion curves of the selected individuals (a) P_A, (b) P_B, and (c) P_C, respectively, from the Pareto front presented in Fig. 10. Complete band gaps are colored in gray. The inset shows the deformation motion of the unit cell at the flat edges defining the band gaps. (For interpretation of the references to color in this figure legend, the reader is referred to the web version of this article.)
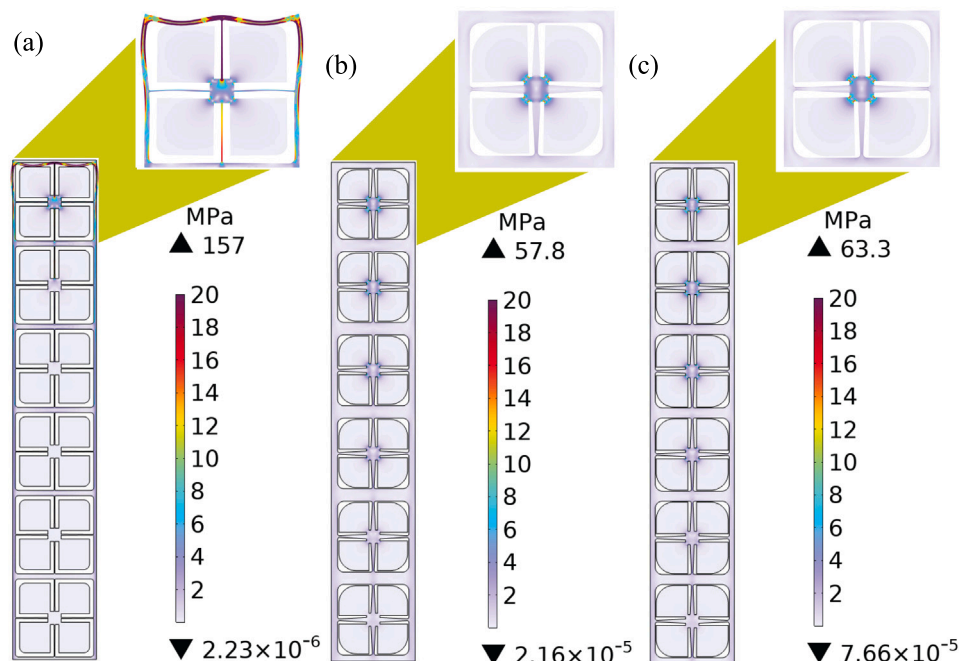
Fig. 12. von Mises stress field obtained in transient analysis of arrays formed by unit cells (a) P_A (b) P_B, and (c) P_C presented in Fig. 10. The stress fields were selected at time steps occurring the maximum von Mises stress for each array. The colormap indicates the variation of Von Mises stress with minimum and maximum values indicated by the triangles. (For interpretation of the references to color in this figure legend, the reader is referred to the web version of this article.)

by impact loads. Our research demonstrates that overlooking stress analysis can yield to structurally unfeasible configurations under such loading conditions. We concurrently obtained unit cell designs attaining comparable vibration attenuation performance and enhanced load resistance, suitable for practical applications.

By using a multi-objective optimization approach, we have generated a set of viable solutions, enabling the selection of the most appropriate design for applications with distinct impact load amplitudes. To confirm the attenuation and mechanical performance of the

metamaterial solutions, future work will focus on the experimental validation through modal impact analysis – to extract the vibration attenuation – and dropped-weight impact testing – to quantify the stress levels. Moreover, the diverse solutions provided by our strategy facilitate the design of graded A/E MM-based structures, significantly expanding the range of wave attenuation. This feature holds immense value, since impact loads are characterized by wide frequency spectrum. Thus, mitigating the adverse effects of impact loads across wide frequency bands is extremely necessary. The exploration of graded A/E
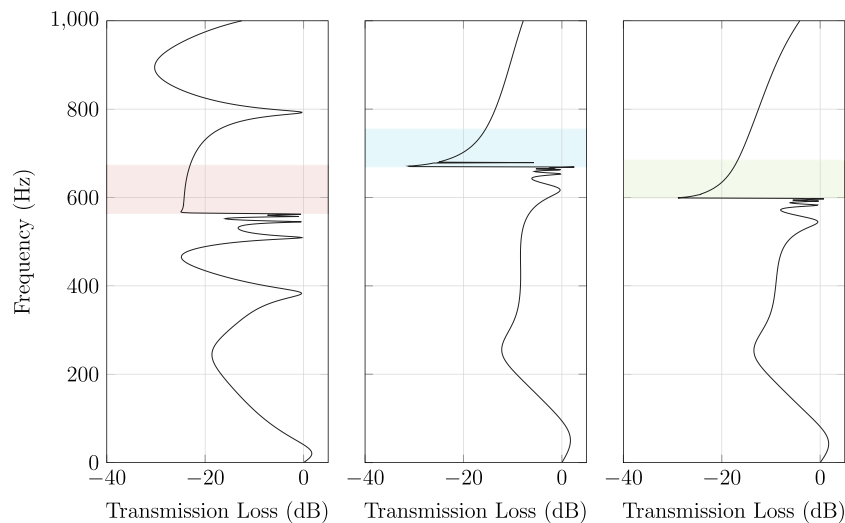
Fig. 13. Transmission loss diagrams for metamaterial plates containing unit cells P_A (left), P_B (middle), and P_C (right) with non-uniform beams (as presented in Fig. 10). The shaded areas indicate the band gap found by solving the EMD and the asymmetric peaks indicate the wave attenuation due to the unit cells' resonance.

MMs for absorbing impact loads will be numerically and experimentally considered in a future work. One of the challenges found in our approach is the computational time demanded by the evaluation of the design variables vector. As a future work, we will combine our optimization strategy with reduced order models (ROMs) that allow a fast calculation of the dynamic properties of the metamaterial. Although numerical damping was introduced to provide solutions with better convergence, it is important to investigate the effect of material damping into the vibration and mechanical performances, which will be addressed in further studies. In essence, our proposed multi-objective design optimization opens new avenues for the development of A/E MMs, enhancing their ability to filter vibration of certain frequencies from structures under challenging impact loading conditions, such as foundations that are installed in onshore and offshore environment through an impact hammer.

CRediT authorship contribution statement

Ana Carolina Azevedo Vasconcelos: Writing – original draft, Methodology, Conceptualization. **Dingena Schott:** Writing – review & editing, Supervision, Project administration. **Jovana Jovanova:** Writing – review & editing, Supervision, Project administration, Funding acquisition, Conceptualization.

Declaration of competing interest

The authors declare that they have no known competing financial interests or personal relationships that could have appeared to influence the work reported in this paper.

Acknowledgment

References

[1] Huang Hsin-Haou, Sun Chin-Teh, Huang Guoliang. On the negative effective mass density in acoustic metamaterials. Internat J Engrg Sci 2009;47(4):610–7.

[2] Hao Li-Mei, Ding Chang-Lin, Zhao Xiao-Peng. Tunable acoustic metamaterial with negative modulus. Appl Phys A 2012;106:807–11.

[3] Zhu Rui, Liu Xiaoning, Hu Gengkai, Sun Chin-Teh, Huang Guoliang. Negative refraction of elastic waves at the deep-subwavelength scale in a single-phase metamaterial. Nat Commun 2014;5(1):1–8.

[4] Liu Zhengyou, Zhang Xixiang, Mao Yiwei, Zhu YY, Yang Zhiyu, Chan Che T, Sheng Ping. Locally resonant sonic materials. Science 2000;289(5485):1734–6.

[5] Zhu Rui, Chen Yangyang, Wang Yue-Sheng, Hu Gengkai, Huang Guoliang. A single-phase elastic hyperbolic metamaterial with anisotropic mass density. J Acoust Soc Am 2016;139(6):3303–10.

[6] Dong Hao-Wen, Zhao Sheng-Dong, Wang Yue-Sheng, Zhang Chuanzeng. Broadband single-phase hyperbolic elastic metamaterials for super-resolution imaging. Sci Rep 2018;8(1):2247.

[7] Gao Penglin, Climente Alfonso, Sánchez-Dehesa José, Wu Linzhi. Single-phase metamaterial plates for broadband vibration suppression at low frequencies. J Sound Vib 2019;444:108–26.

[8] Elmadih Waiel, Chronopoulos Dimitrios, Syam Wahyudin P, Maskery Ian, Meng Han, Leach Richard K. Three-dimensional resonating metamaterials for low-frequency vibration attenuation. Sci Rep 2019;9(1):1–8.

[9] Tan Kwek Tze, Huang Hsin-Haou, Sun Chin-Teh. Blast-wave impact mitigation using negative effective mass density concept of elastic metamaterials. Int J Impact Eng 2014;64:20–9.

[10] Khan Mahfujul H, Li Bing, Tan Kwek-Tze. Impact load wave transmission in elastic metamaterials. Int J Impact Eng 2018;118:50–9.

[11] Vo Nhi H, Pham Thong M, Hao Hong, Bi Kaiming, Chen Wensu, San Ha Ngoc. Blast resistant enhancement of meta-panels using multiple types of resonators. Int J Mech Sci 2022;215:106965.

[12] Wang Pai, Casadei Filippo, Shan Sicong, Weaver James C, Bertoldi Katia. Harnessing buckling to design tunable locally resonant acoustic metamaterials. Phys Rev Lett 2014;113(1):014301.

[13] Bertoldi Katia. Harnessing instabilities to design tunable architected cellular materials. Annu Rev Mater Res 2017;47:51–61.

[14] Oh Joo Hwan, Ahn Young Kwan, Kim Yoon Young. Maximization of operating frequency ranges of hyperbolic elastic metamaterials by topology optimization. Struct Multidiscip Optim 2015;52:1023–40.

[15] Christiansen Rasmus E, Sigmund Ole. Designing meta material slabs exhibiting negative refraction using topology optimization. Struct Multidiscip Optim 2016;54:469–82.

[16] Lu Lirong, Yamamoto Takashi, Otomori Masaki, Yamada Takayuki, Izui Kazuhiro, Nishiwaki Shinji. Topology optimization of an acoustic metamaterial with negative bulk modulus using local resonance. Finite Elem Anal Des 2013;72:1–12.

[17] Noguchi Yuki, Matsushima Kei, Yamada Takayuki. Level set-based topology optimization for the design of labyrinthine acoustic metamaterials. Mater Des 2022;219:110832.

[18] Dong Hao-Wen, Zhao Sheng-Dong, Wang Yue-Sheng, Zhang Chuanzeng. Topology optimization of anisotropic broadband double-negative elastic metamaterials. J Mech Phys Solids 2017;105:54–80.

[19] Lin XY, Li Eric, He Zhicheng, Wu Yi, Li Qiqi. Design of single-phase chiral metamaterials for broadband double negativity via shape optimization. Appl Math Model 2021;91:335–57.

[20] Abdeljaber Osama, Avci Onur, Inman Daniel J. Optimization of chiral lattice based metastructures for broadband vibration suppression using genetic algorithms. J Sound Vib 2016;369:50–62.

[21] Wu Kun, Hu Haiyan, Wang Lifeng, Gao Yuqiang. Parametric optimization of an aperiodic metastructure based on genetic algorithm. Int J Mech Sci 2022;214:106878.

[22] Panahi Emad, Hosseinkhani Ali, Frangi Attilio, Younesian Davood, Zega Valentina. A novel low-frequency multi-bandgaps metaplate: Genetic algorithm based optimization and experimental validation. Mech Syst Signal Process 2022;181:109495.

[23] Yan Gengwang, Yao Song, Li Yingli, Zhou Wenxi. Topological optimization of thin elastic metamaterial plates for ultrawide flexural vibration bandgaps. Int J Mech Sci 2023;242:108014.

[24] Thomes Renan L, Mosquera-Sánchez Jaime A, De Marqui Jr Carlos. Bandgap widening by optimized disorder in one-dimensional locally resonant piezoelectric metamaterials. J Sound Vib 2021;512:116369.

[25] Jian Yupei, Tang Lihua, Hu Guobiao, Wang Yuesheng, Aw Kean C. Adaptive genetic algorithm enabled tailoring of piezoelectric metamaterials for optimal vibration attenuation. Smart Mater Struct 2022;31(7):075026.

[26] Gao Yuqiang, Wang Lifeng. Broad bandgap active metamaterials with optimal time-delayed control. Int J Mech Sci 2023;254:108449.

[27] Liu Xiaoning, Hu Gengkai, Sun Chin-Teh, Huang Guoliang. Wave propagation characterization and design of two-dimensional elastic chiral metacomposite. J Sound Vib 2011;330(11):2536–53.

[28] Yang Xiong Wei, Lee Joong Seok, Kim Yoon Young. Effective mass density based topology optimization of locally resonant acoustic metamaterials for bandgap maximization. J Sound Vib 2016;383:89–107.

[29] Milton Graeme W, Willis John R. On modifications of Newton's second law and linear continuum elastodynamics. Proc R Soc A: Math Phys Eng Sci 2007;463(2079):855–80.

[30] Van Belle Lucas, Claeys Claus, Deckers Elke, Desmet Wim. On the impact of damping on the dispersion curves of a locally resonant metamaterial: Modelling and experimental validation. J Sound Vib 2017;409:1–23.

[31] DE Goldberg. Genetic algorithms in search. optimization, and machine learning. Addison Wesley; 1989.

[32] Hussein Mahmoud I, Leamy Michael J, Ruzzene Massimo. Dynamics of phononic materials and structures: Historical origins, recent progress, and future outlook. Appl Mech Rev 2014;66(4).